Hall Thruster Near-Field Plume Characterization Through Optical Emission Spectroscopy

IEPC-2019-246

Presented at the 36th International Electric Propulsion Conference
Vienna, Austria
September 15–20, 2019

Michael R. Nakles* and Taylor S. Matlock†
The Aerospace Corporation, El Segundo, CA, 90245

Spontaneous emission of xenon at five near-infrared wavelengths, corresponding to de-excitation of neutral atoms from the $2p$ (Paschen notation) manifold, was measured in the near-field of a 1 kW laboratory Hall thruster plume to non-intrusively measure excited state neutral densities and make predictions of electron temperature through the application of the KCD collisional radiative model. The measurements were taken between the exit plane of the thruster and the cathode orifice so that the asymmetric cathode bridge region of the plume could be studied. Inverse Radon transforms of the line-of-sight irradiance measurements were performed using the filtered back projection technique for 2D analysis and compared with 1D analysis from an Abel inversion. Electron temperature predictions were made by fitting the modeled radiant power density to the experimental measurements using a least squares fit with up to five lines. Resulting temperature distributions agreed well with recent Langmuir probe measurements near the discharge channel, however line intensities were poorly fit by the KCD model elsewhere including the cathode bridge. The non-physical results of the model in these regions may be due to higher uncertainty of the experimental inputs (measurement uncertainty and numerical artifacts from tomographic inversion) and the existence of a non-Maxwellian or multi-peaked electron energy distribution function, which was not accounted for in the emission excitation rates used in the model. The tomographic analysis of the measurements show that the inversion techniques are useful for optically studying the Hall thruster near-plume and the results can be improved with a higher angular sampling resolution.

Nomenclature

a	semi-empirical fit parameter used to calculate zero-pressure extrapolated cross sections (see Ref. 1)
A_{ij}	Einstein coefficient
c	speed of light in vacuum
$c(\lambda)$	calibration factor for optical system to convert counts to absolute spectral irradiance
CRM	collisional radiative model
e	elementary charge
E_e	electron energy
E_1	singly-charged ion energy
E_2	doubly-charged ion energy
ICCD	intensified charge-coupled device
I_i^{CRM}	normalized best-fit modeled line intensity
I_i^{exp}	normalized experimental line intensity
$I_L(\lambda)$	absolute spectral irradiance from calibration lamp
I_λ	irradiance at wavelength λ
f	distribution function

*Propulsion Test Engineer, The Aerospace Corporation, 2310 E. El Segundo Blvd., El Segundo, CA 90245
†Member of Technical Staff, The Aerospace Corporation, 2310 E. El Segundo Blvd., El Segundo, CA 90245

f_s	sensitivity factor for standard deviation of predicted electron temperature
h	Planck's constant
J_λ	radiant power per unit volume at wavelength λ
k	Boltzmann constant
k_{em}^λ	metastable-state atom electron-impact emission excitation rate coefficient
k_{e0}^λ	ground-state atom electron-impact emission excitation rate coefficient
k_1^λ	singly-charged ion-impact emission excitation rate coefficient
k_2^λ	doubly-charged ion-impact emission excitation rate coefficient
K_λ	sum of population scaled emission excitation rates
m_e	electron mass
$\dot{m}_a$	anode propellant mass flow rate
$\dot{m}_c$	cathode propellant mass flow rate
M	atomic mass
n	semi-empirical fit parameter used to calculate zero-pressure extrapolated cross sections (see Ref. 1)
n	number of lines used in multi-line intensity fit of CRM with experimental data
n_t	number of irradiance measurements made along t axis
n_θ	number of viewing angles in irradiance measurements
N_e	electron density
N_m	metastable-state atom density
N_0	ground-state neutral atom density
N_1	singly-charged ion density
N_2	doubly-charged ion density
r	spatial coordinate or radial coordinate about thruster axis (z-axis)
$R_s(\lambda)$	reflectance of Spectralon disk used in optical system calibration
$S(\lambda)$	signal measured by the ICCD in counts
t	axis of optical detector motion (see Fig. 3)
P	pressure
q	multiple for units of elementary charge
v	velocity
V	ion acceleration voltage
x	axis in thruster coordinate system perpendicular to the cathode plane (see Fig. 3)
y	axis in thruster coordinate system in the cathode plane (see Fig. 3)
z	axis in thruster coordinate system in thrust direction (see Fig. 3)
α	ratio of singly charged ion density to total ion density ($= N_1/N_e = N_1/(N_1 + 2N_2)$)
γ	semi-empirical fit parameter used to calculate zero-pressure extrapolated cross sections (see Ref. 1)
$\delta I_{\mathrm{CRM}}^2$	relative error for least squares fit of CRM to experimental data for an emission line
Δt	spacing between irradiance measurements along t axis
$\Delta\theta$	angular increment between viewing angles in irradiance measurements
θ	viewing angle of detector for irradiance measurement (see Fig. 3)
θ_d	viewing angle of optical detector relative to surface target during calibration
λ	wavelength
σ_{T_e}	standard deviation of predicted electron temperature
σ_{J_λ}	standard deviation of measured line intensity
σ_{em}^λ	metastable-state atom electron-impact line emission excitation cross section
σ_{e0}^λ	ground-state atom electron-impact line emission excitation cross section
σ_1^λ	singly-charged ion impact line emission excitation cross section
σ_2^λ	doubly-charged ion impact line emission excitation cross section
χ^2	least squares sum to minimize for fitting CRM intensity to experimental values
$\mathcal{R}$	Radon transform

Introduction

NEAR-plume characterization of Hall effect thrusters is important for studying their fundamental physics including the ionization and acceleration mechanisms, but is difficult to perform experimentally due to numerous challenges that this environment imposes on diagnostics. The physical presence of probes significantly perturbs the local plasma so that the properties of interest are changed at the probe/plasma interface and these perturbations can also cause fundamentally different operation of the thruster. The high ion flux impinging on the probe is largely neutralized and may be lead to ingestion effects similar to increased facility background pressure. Sputtered metal from probe surfaces can be also be a source of non-propellant species neutrals and ions complicating analysis. The ion impacts also produce secondary electrons and probe heating that affect measured probe current. Analysis of probe data often is based on theory that assumes a symmetrical sheath around the probe. The divergent flow near the thruster exit plane precludes the ability to position a probe without inducing wakes resulting in sheath asymmetry. Strong magnetic fields near the exit plane are often not accounted for in probe analysis. Even when accounting for magnetic field effects, the electron cross-field mobility must be known a priori.[2]

In comparison with the probes, which disrupt the near-field plasma environment, optical diagnostics are attractive due to their non-intrusive nature. Measurement of atomic emission can enable calculations of electron energy distribution and particle densities. However, these calculations require the employment of a collisonial radiative model (CRM), which is a simplification of a complex system of the population and depopulation of atomic energy states that relies on knowledge of collision cross sections that often have high levels of measurement uncertainty or have not been measured at all.

In this study, we explore the application of a collisional radiative model to optical emission spectroscopy measurements in the near-field plume of a laboratory Hall effect thruster to predict electron temperature. We also explore the use of tomography to spatially resolve the line-of-sight optical measurements to study asymmetrical features arising from the externally mounted cathode.

Collisional Radiative Model

A collisional radiative model calculates the population dynamics of atomic states in a plasma by quantifying and summing the rates of radiative and collisional transitions into and out of these states. Due to the large number of possible transition pathways and the fact that many of the relevant excitation collision cross sections are unknown, the model simplifies the physical system by only incorporating the most probable transitions on relevant time scales.[3] These models can be used to predict the spectral emission of the plasma from the radiative decay processes.

A collisional radiative model for studying near-infrared emissions from excited neutral atoms in xenon plasma for electric propulsion devices was developed by Karabadzhak et al.[4] incorporating experimentally measured apparent emission excitation cross sections from Chiu et al.[1] This CRM, known as the KCD model, accounts for population of excited states from electron collisions with ground-state atoms and metastable neutral atoms as well as collisions of singly and doubly-charged ions with ground-state atoms. Depopulation is accounted for solely from radiative transitions, neglecting quenching electron collisions due to the fact their frequency is comparatively small at plasma conditions typical of a Hall thruster plume.[4] The model can be formulated as[4]

$$J_\lambda(\mathrm{Xe_I}) = \frac{hc}{\lambda} N_0 N_e \left(k_{e0}^\lambda + \frac{N_m}{N_0} k_{em}^\lambda + \alpha \cdot k_1^\lambda + \frac{1-\alpha}{2} k_2^\lambda \right) = \frac{hc}{\lambda} N_0 N_e K_\lambda(T_e, \alpha, P) \tag{1}$$

where the factor in brackets, referred to as K_λ in this work, is the summation of the apparent emission excitation rates multiplied by scaling factors to account for the population of various species involved in the collisions. This factor is a function of electron energy distribution, ion charge state fraction, and pressure (due to radiation trapping effects on emission excitation cross sections). In the present study, J_λ is the radiant power density (W/cm^3) of a volumetric element of plasma at wavelength λ.

This CRM was designed to model eleven near-infrared emission lines from radiative decay out of the xenon $2p$ (Paschen notation) manifold,[5] some of which are relatively bright and convenient for experimental measurement due to their high Einstein coefficients. Table 1 summarizes the lines included in the KCD CRM. Five of these lines are from radiative decay to the $1s_5$ metastable state and the others decay to the resonant $1s_2$ and $1s_4$ levels, which are directly optically coupled to the ground-state. The $1s_5$ metastable state has a long lifetime and is close in energy to the $2p_i$ levels, which leads to high excitation rates out of this level. For upper states with a transition that decays to the $1s_5$ metastable state, the second term in the brackets of Eq. 1 makes a significant contribution to the radiated emission, but for the other transitions this term can be neglected when the population of metastable atoms is less than about 1%,[4] which should be true in most cases for low temperature Hall effect thruster plumes.[5] Excitation from the other metastable state, $1s_3$, is neglected due to its comparatively low population, making $1s_5$ the only metastable state that contributes to emission in the CRM.[5]

λ (nm)	Transition Level		Transition Energy (eV)			A_{21} (10^6 s^{-1})	Branching Ratio
	Upper	Lower	Upper	Lower	ΔE	(from Ref. 6)	(from Ref. 7)
788.7[a,b]	$2p_1$	$1s_2$	11.141	9.570	1.571	35	0.719
820.6[c]	$2p_4$	$1s_3$	10.958	9.447	1.510	20	0.413
823.2[a,b,c]	$2p_6$	$1s_5$	9.821	8.315	1.506	28.6	0.743
826.7[c]	$2p_2$	$1s_2$	11.069	9.570	1.499	16.2	0.307
828.0[a,b,c]	$2p_5$	$1s_4$	9.933	8.437	1.497	36.9	0.998
834.7[a,b,c]	$2p_3$	$1s_2$	11.055	9.570	1.485	42	0.863
840.9[a]	$2p_7$	$1s_5$	9.789	8.315	1.474	3.06	0.099
916.3[a,b]	$2p_7$	$1s_4$	9.789	8.437	1.353	24	0.901
881.9[a,b]	$2p_8$	$1s_5$	9.721	8.315	1.405	30.0	1.000
895.2[a]	$2p_6$	$1s_4$	9.821	8.437	1.385	8.1	0.243
904.5[a,b]	$2p_9$	$1s_5$	9.686	8.315	1.370	12.4	0.379
980.0[a,b]	$2p_{10}$	$1s_5$	9.580	8.315	1.265	31.1	0.975
992.3[a]	$2p_9$	$1s_4$	9.686	8.437	1.249	13.0	0.621

Table 1: Near-infrared xenon neutral atomic emission lines from the $2p$ manifold used in optical emission spectroscopy and collisional radiative modeling. Superscripts: a=included in the KCD model, b=apparent emission excitation cross section experimentally measured in Ref. 1, c=line measured in the present study

The emission excitation rate coefficients are calculated as the product of apparent emission excitation cross section and velocity (assuming isotropic velocity) integrated over the electron energy distribution as[8]

$$k_{ij}^{\lambda} = < \sigma_{ij}^{\lambda} v_i >_{E_i} = \int_0^{\infty} f(E_i)\sigma_{ij}^{\lambda}(E_i)v_i(E_i)dE_i \tag{2}$$

For Hall effect thruster analysis, a Maxwellian electron energy distribution is usually assumed so that Eq. 2 can be written as[1]

$$k_{ej}^{\lambda} = \int_0^{\infty} 2E_e\sqrt{\frac{2}{\pi(kT_e)^3 m_e}}\exp\Big(-\frac{E_e}{kT_e}\Big)\sigma_{ej}^{\lambda}(E_e)dE_e \tag{3}$$

Ion impact emission excitation cross section measurements from Chiu et al.[1] and Sommerville et al.[9] show that variation of cross section with energy is smooth with a relatively small slope for energies typical of a Hall effect thruster plume[4] and therefore are approximated as being constant over the ion velocity distribution of plume. Thus, ion impact emission excitation rate coefficients can be calculated as[4]

$$k_1^{\lambda} \approx \sigma_1^{\lambda}(E_1)\sqrt{\frac{2eV}{M}} \tag{4}$$

and

$$k_2^{\lambda} \approx \sigma_2^{\lambda}(E_2)\sqrt{\frac{4eV}{M}} \tag{5}$$

Due to the low fraction of metastable atoms in the plume and the assumption of similar emission excitation cross sections for ground-state and metastable atoms, ion impact emission excitation from metastable states is neglected.[5] Analysis from Sommerville et al.[9] demonstrates that ion impact excitation makes a significant contribution to emission for electric propulsion device plumes when the electron temperature is low.

The $1s_5$ metastable fraction is modeled using a steady-state equilibrium of population from the decay of $2p_i$ levels into $1s_5$ and depopulation through excitement from the $1s_5$ level to $2p_i$ levels followed by subsequent decay to the $1s_4$ level. Depopulation in the model also includes excitement from $1s_5$ to other atomic manifolds, from which repopulation of the $1s_5$ state from optical transitions is negligible.[5] Due to the lack of known emission collision cross sections from the metastable state to the $2p_i$ levels at the time, Karabadzhak et al.[4] approximated them using branching probabilities and the degeneracy of the $2p_i$ upper state. However, after some excitation cross sections from the metastable state were experimentally measured by Jung[10] and computational methods were developed to calculate metastable excitation cross sections,[11,12] Dressler et al.[5] updated the KCD model to include a metastable fraction calculation using these newly available data. The updated model showed an improved fit to experimental data and showed that the old method for metastable fraction approximation resulted in an overestimation. Despite the fact that a direct calculation can now be performed, the metastable fraction term remains one of the most uncertain parameters in the KCD model due to the large number of cross sections involved in its calculation and the incompleteness of the experimentally determined cross sections.

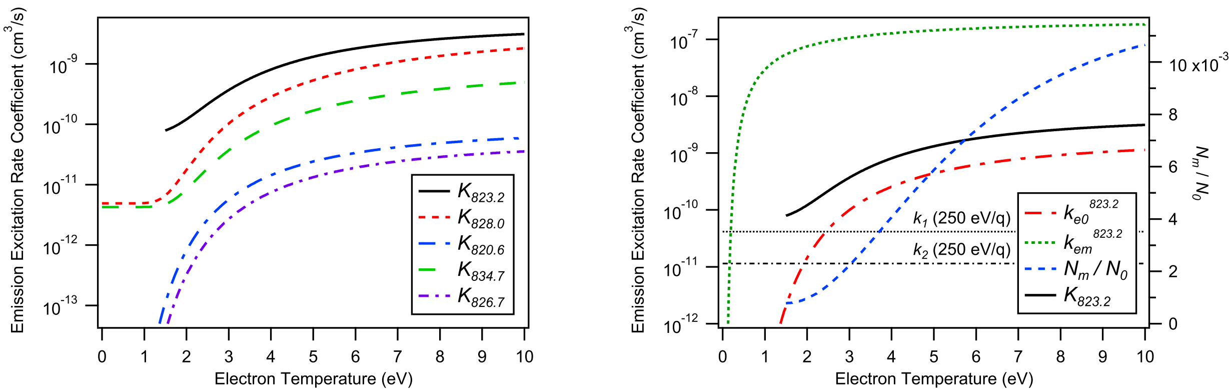

(a) Population-scaled emission excitation rate summation, K_λ, (see Eq. 1) of emission lines.

(b) 823.2 nm emission excitation rates and $K_{823.2}$. N_m/N_0 as a function of electron temperature was calculated by Dressler et al.[5]

Figure 1: Emission excitation rates for the lines measured in the present study were calculated assuming a Maxellian electron energy distribution, $\alpha = 0.8$, and an ion energy per charge of 250 eV/q.

λ (nm)	σ^λ_{em}	σ^λ_1, σ^λ_2	σ^λ_{e0}	a	n	γ
820.6	-	X	Ref. 7^a	2.659	8	0.92
823.2	Ref. 10^a	Ref. 9	Ref. 1	1.356^b	15^b	0.65^b
826.7	-	X	Ref. 7^a	5.357	25	1.20
828.0	-	Ref. 9	Ref. 1	1.297^b	16^b	1.47^b
834.7	-	Ref. 9	Ref. 1	0.275^b	8^b	2.00^b

Table 2: References for experimentally measured emission excitation cross sections used to calculate emission excitation rates and fit parameters used to calculate zero-pressure extrapolated ground-state atom electron-impact emission excitation cross sections (see Ref. 1). a=excitation cross section given, multiplied by branching fraction from Ref. 7 to calculate *emission* excitation cross section, b=from Ref. 1, -=N/A, X=not available and neglected in this study.

Figure 1a shows the population-scaled emission excitation rate summation, K_λ, for the emission lines measured in the present study at conditions typical of a 300 V Hall effect thruster ($\alpha = 0.8$ and an ion energy per charge of 250 eV/q). The sources of experimentally measured cross section data used in their calculation are summarized in Table 2. The ground-state atom electron-impact emission excitation cross sections were zero-pressure extrapolated from experimental data using the semi-empirical method described in Ref. 1. Calculations were made with apparent cross sections to include the populating contribution of radiative cascades from higher energy states. The excitation rates for electron collisions with ground-state and metastable-state atoms, k_{e0} and k_{em}, were calculated assuming a Maxwellian electron energy distribution.

Figure 1b shows the 823.2 nm emission excitation rates for the collisions modeled in the CRM and illustrates the strong effect of metastable excitation on $K_{823.2}$. The metastable state population fraction, N_m/N_0 as a function of electron temperature was calculated by Dressler et al.[5] for 250 V ions using modeled cross sections from the Breit-Pauli B-Spline R-matrix (BSR) method,[13] the relativistic distorted-wave approximation method[12] and Born calculations[14] in addition to experimentally measured cross section data.[10]

The KCD model can be used to predict electron temperature from experimental measurements of emission intensity in a thruster plume. The simplest method involves using Eq. 1 to calculate the predicted ratio of intensity of two emission lines as a function of electron temperature (Eq. 6). The predicted temperature is found from the point on the modeled curve that corresponds to the experimentally measured two-line intensity ratio.

$$\frac{J_{\lambda 1}}{J_{\lambda 2}}(T_e) = \frac{\lambda_2}{\lambda_1}\frac{K_{\lambda 1}}{K_{\lambda 2}} \tag{6}$$

Ratios involving the bright emission lines of 823.2, 828.0, and 834.7 nm are often used for this two-line temperature analysis.[4,5,15,16] Figure 2 shows ratios of 823.2/828.0 and 834.7/828.0 nm emission calculated for a 300 V Hall thruster ($\alpha = 0.8$ and 250 eV/q ions).

These curves show that error in the measured intensity ratio leads to increasing uncertainty in electron temperature prediction for increasing values of electron temperature. A propagation of uncertainty analysis shows that the standard deviation of electron temperature prediction, σ_{T_e}, is given by Eq. 7. The sensitivity factor, f_s, normalized to electron temperature is also plotted in Fig. 2 to illustrate how the sensitivity of σ_{T_e} to uncertainty in measured line intensity propagates with increasing temperature. Note that this propagation of uncertainty analysis only encompasses errors in emission line intensity measurements and not uncertainty in the emission excitation cross section data used to generate the line ratio vs. electron temperature curves, which is higher at low values of electron energy.

The use of 834.7/828.0 nm ratio avoids the uncertainty from the metastable population and metastable excitation emission cross section terms in the CRM. However, as shown in Fig. 2, the temperature prediction is 2-3× more sensitive to relative error in measured line intensity than the 823.2/828.0 nm curve.

$$\sigma_{T_e}(T_e) = \frac{J_{\lambda 1}}{J_{\lambda 2}}(T_e)\frac{\partial T_e}{\partial(J_{\lambda 1}/J_{\lambda 2})}(T_e)\sqrt{\left(\frac{\sigma_{J_{\lambda 1}}}{J_{\lambda 1}}\right)^2 + \left(\frac{\sigma_{J_{\lambda 2}}}{J_{\lambda 2}}\right)^2} = f_s(T_e)\sqrt{\left(\frac{\sigma_{J_{\lambda 1}}}{J_{\lambda 1}}\right)^2 + \left(\frac{\sigma_{J_{\lambda 2}}}{J_{\lambda 2}}\right)^2} \tag{7}$$

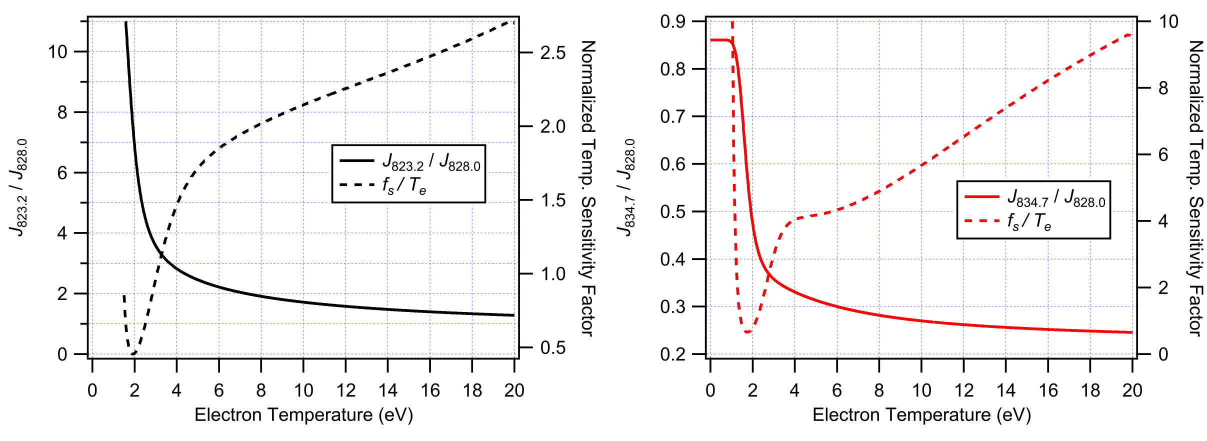

(a) 823.2/828.0 nm line intensity ratio. (b) 834.7/828.0 nm line intensity ratio.

Figure 2: Emission line intensity ratios as a function of electron temperature predicted for a 300 V Hall thruster.[4,5] The sensitivity factor shows how the standard deviation in predicted electron temperature responds to uncertainty in intensity measurements.

When more than two emission lines are measured, a multi-line fit can be performed to find the model temperature that results in the lowest error between the normalized measured and modeled intensity values where the least-squares sum is minimized in Eq. 8.[5] Fitting the model to more measured emission lines generally improves the accuracy of the electron temperature prediction.

$$\chi^2 = \frac{1}{n}\sum_{i=1}^{n}\frac{(I_i^{\text{exp}} - I_i^{\text{CRM}})^2}{(I_i^{\text{exp}})^2}$$
$$\sum_{i=1}^{n} I^{\text{exp}} = \sum_{i=1}^{n} I^{\text{CRM}} = 1 \tag{8}$$

Tomographic Techniques

The radiant power density, $J_\lambda(r)$, predicted by the CRM is directly proportional to the density of the upper-level state and the Einstein coefficient for the specific transition and is given as[3]

$$J_\lambda(r) = \frac{hc}{\lambda} N_i(r) A_{ij} \tag{9}$$

In order to experimentally determine $J_\lambda(r)$, measurements of line-of-sight integrated radiant power per area (irradiance) are transformed via tomographic methods. For an optically thin plasma, irradiance measured by a collimated detector is the integral of $J_\lambda(r)$ along the line of sight of the collection optic.

In the case of a cylindrically symmetric plasma, a set of side-on irradiance measurements spanning at least half the diameter of the plasma column can be used to find J_λ as a function of radius. The irradiance is described by the forward Abel transform as[3]

$$I_\lambda(y) = 2\int_y^R \frac{J_\lambda(r) r dr}{\sqrt{r^2 - y^2}} \tag{10}$$

An Abel inversion can be applied to these irradiance measurements to find the radiant power density as a function of radius. The analytical formula for the inverse Abel transform is[3]

$$J_\lambda(r) = -\frac{1}{\pi}\int_r^R \frac{dI_\lambda(y)}{dy}\frac{dy}{\sqrt{y^2 - r^2}} \tag{11}$$

In practice, it is difficult to directly calculate the radiant power density from Eq. 11 using experimental data due to the ill-posed nature of the solution. The spatial derivative of the forward transform is highly sensitive to noise or error in the data. The error accumulates as the range of the integral increases for locations nearing the center of the domain. Various numerical techniques have been proposed to invert experimental data.[17] In the present study, the method described in Ref. 15 was employed using a least-squares fit with no regularization due to the sparse nature of the data set, which counteracted the effect of noise in the solution.

When there is asymmetry in the plasma, an inverse Radon transform can be used to spatially resolve $J_\lambda(x, y)$ within the measurement plane. An inverse Radon transform can be performed on multiple sets of parallel side-on line-of-sight measurements taken at different viewing angles as depicted in Fig. 3. In this study, irradiance measurements are taken at multiple positions along the detector motion axis, t, for rotations of a Hall thruster about its central axis for views at various values of θ. The $I(t, \theta)$, measurements (referred to as a sinogram) are the Radon transform of $J_\lambda(x, y)$ as shown in Eqs. 12 and 13.[3] An inverse Radon transform can be performed through various numerical methods including filtered back projection, used in this study, and various algebraic reconstruction techniques.[18] Figure 4 shows a sinogram for a simple Hall thruster plume model and its inverse Radon transform.

$$I_\lambda(t, \theta) = \mathcal{R}_2\left\{J_\lambda(x, y)\right\} \tag{12}$$

$$J_\lambda(x, y) = \mathcal{R}_2^{-1}\left\{I_\lambda(t, \theta)\right\} \tag{13}$$

The filtered back projection method involves taking the fast Fourier transforms of the parallel line-integrated measurements, convolving them with a filter function to account for the spacing of the polar measurement grid and to suppress noise, then back projecting them from the frequency domain them in additive fashion onto a spatial Cartesian grid. It is described in detail in Ref. 18. In the present study, the ramp (Ram-Lak) filter with no windowing was used due to the minimal effects of noise on the reconstruction of the sparse data set.

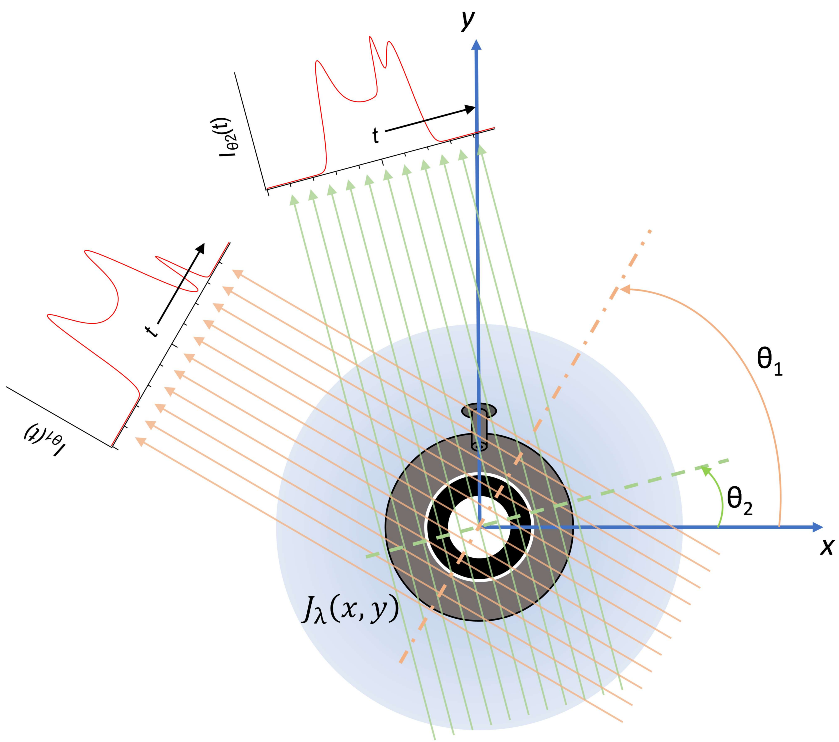

Figure 3: Illustration showing how irradiance measurements made from a detector scanning along axis t at various viewing angles θ are used to measure the Radon transform of $J_\lambda(x, y)$. (Figure adapted from Ref. 18.)

Experimental Apparatus and Techniques

Hall Effect Thruster

A 1 kW (nominal) laboratory thruster made by Princeton Plasma Physics Laboratory[19] (Fig. 6) was used in this study. The discharge channel has an outer diameter of 90 mm, an inner diameter of 54 mm, and a channel depth of 49 mm. The thruster has two concentric magnet circuits; an inner circuit around the center pole piece, and an outer circuit around the outer perimeter of the discharge channel. The inner magnetic pole is covered by a 3.2 mm thick ceramic cap, while the outer pole is an exposed conducting surface. A HeatWave hollow cathode is mounted at the 12 o'clock position with a declination angle of 50° relative to thruster axis. The cathode orifice is located 27 mm downstream of the outer insulator ($z = 0$ in the thruster coordinate system for this study) at a radius of 74 mm from thruster centerline. For a 500 W operating condition, the thruster has been characterized to have a thrust of 25 mN with a specific impulse of 1300 s, yielding an anode efficiency of 30%.[20]

Analog mass flow controllers from MKS were used to control the propellant flow rate to the cathode and anode and TDK-Lambda power supplies were used to power the thruster discharge, magnets, and cathode heater and keeper. The discharge power supply was equipped with an LC filter with a 125 μH inductor between the high side of the power supply and a 23 μF capacitor. A computer data acquisition system recorded the potential and current outputs of the power supplies at a rate of approximately 0.5 Hz.

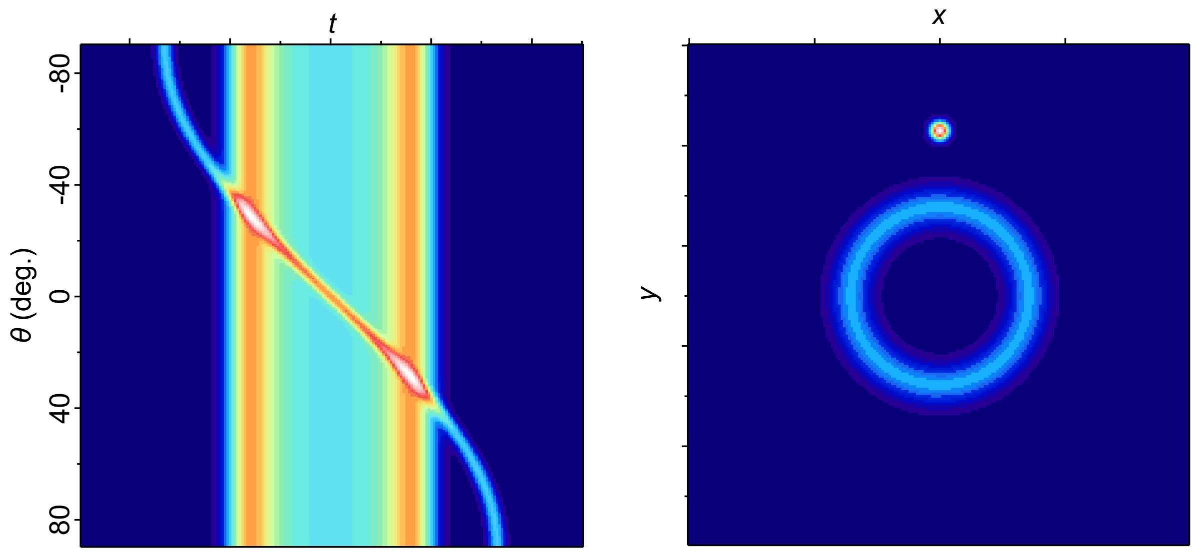

(a) $I_\lambda(t, \theta)$, the Radon transform of $J_\lambda(x, y)$ (displayed as a sinogram).

(b) $J_\lambda(x, y)$, the inverse Radon transform of $I_\lambda(t, \theta)$ reconstructed using the filtered back projection method.

Figure 4: The Radon transform of a simple Hall thruster plume model (phantom) and its reconstruction (inverse Radon transform) using the filtered back projection method.

Test Facility

This study was performed in the EP2 vacuum chamber at The Aerospace Corporation. EP2 is a cylindrical non-magnetic stainless steel vacuum chamber 2.4 m in diameter and 9.8 m in length. Pumping is provided by ten PHPK cryogenic pumps (four 1.2 m flanged cryotubs and six 1.2 m re-entrant pumps). These two stage pumps have a liquid nitrogen baffle (70 K) and a helium cryosail (15 K) and in aggregate provide a maximum measured chamber pumping speed on xenon of about 250 kL/s. Chamber pressure is monitored with two Granville Phillips Stabil-ion gauges. One gauge is mounted on the chamber wall near the longitudinal location of the thruster. The other gauge is mounted inside the chamber near the thruster and is configured to measure background pressure near the exit plane. The gauge is mounted on a 2.75 in. conflat tee with a mesh covered opening pointing upstream of the thruster exit plane, the opposite side capped, and the gauge mounted perpendicularly as described in Ref. 21. In this study the internal gauge was mounted 49.5 cm laterally from the thruster centerline and 3.5 cm upstream of the exit plane (see Fig. 6).

Experimental Setup

This experiment was designed to measure the absolute irradiance from five Xe I atomic emission lines on a detector swept along a lateral path relative to the thruster plume for various rotations of the thruster about its central axis. These irradiance measurements were used to spatially determine the radiant power density through tomographic techniques. The radiant power density was fit to the KCD CRM to predict electron temperature. The experimental setup is shown schematically in Fig. 5. A photograph of the internal chamber configuration is shown in Fig. 6.

The collimator was moved with a two-axis stepper motor positioning system. The t-stage provided lateral motion across the plume and the z-stage controlled the downstream position. A rotary θ-stage provided 180° of thruster rotation necessary for tomography.

Emission was collected by a 12 mm diameter reflective collimator that was fitted with a 6.35 mm diameter entrance aperture to increase the spatial resolution of the measurements. The collector was mounted on the t-stage at a distance of 37.7 cm beneath the thruster centerline. The collimator output was fed into a 200 μm diameter, 0.22 NA fiber that passed through a potted vacuum feed through. The air side end of the fiber

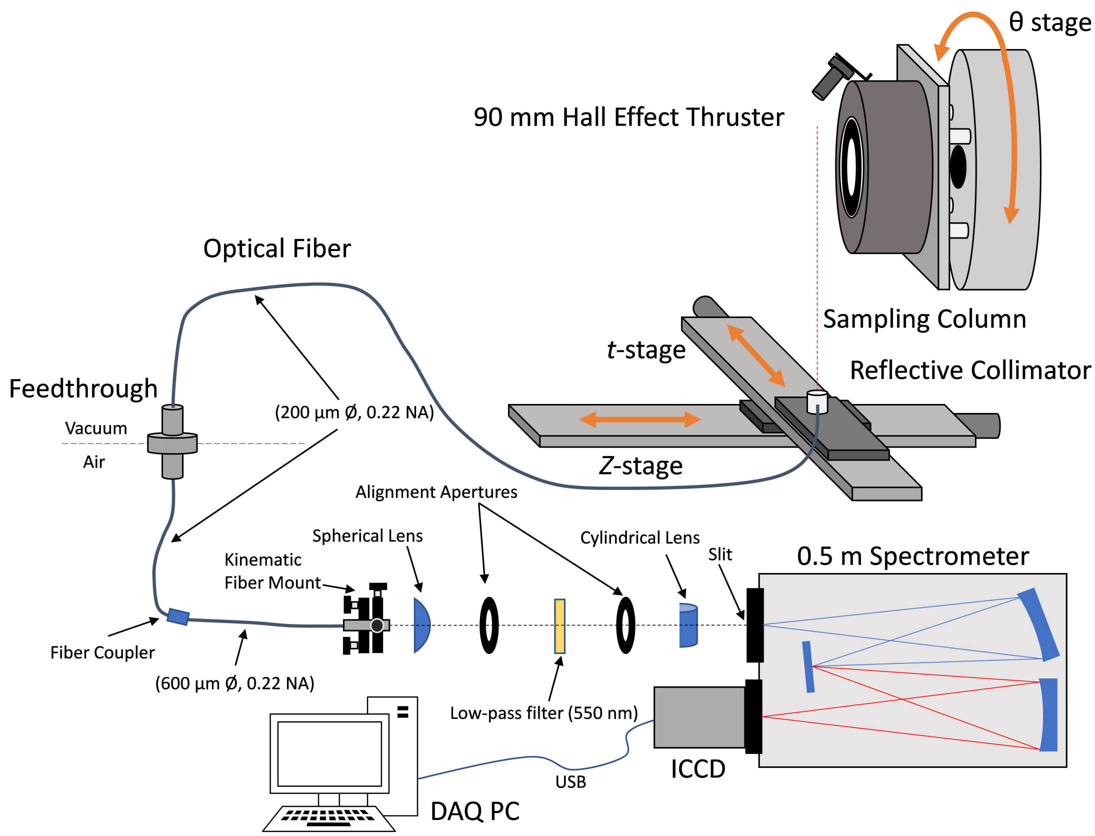

Figure 5: Optical emission spectroscopy measurement setup designed for measuring irradiance on a collimated detector for various viewing angles of the near-field plume about the thruster centerline.

feed through was coupled with a 600 μm diameter, 0.22 NA fiber that brought the signal to an optical bench top. The end of the 600 μm fiber was attached to a kinematic mount and its output was collimated with a spherical lens before traveling through a low-pass filter to ensure that harmonics from the higher frequency light would not be superimposed on the measured spectra. A cylindrical lens focused the beam into a linear shape to match the slit entrance of the spectrometer. Two adjustable apertures were used to help align the beam with the entrance slit. The spectrometer was a 0.5 m f/4 SPEX 500. Its output was measured with a 16 bit ICCD (Andor iStar 334T) used with the maximum gain setting. The measured spectra had a resolution of 0.2 nm.

The optical system as a whole was calibrated so that the ICCD signal in counts could be converted into measurements of absolute spectral irradiance (W/cm^2-nm). During the system calibration, a 1 kW standard of spectral irradiance FEL lamp illuminated a 92 mm diameter Spectralon disk with a reflectance, $R_s(\lambda)$, greater than 98% placed at a distance of 50 cm from the lamp filament with a known spectral irradiance, $I_L(\lambda)$ (W/cm^2-nm). The reflective collimator viewed the center of the disk at an angle of 11.3°. An optical system calibration factor as a function of wavelength was determined by dividing the known spectral irradiance viewed by the detector by the signal, $S(\lambda)$, measured by the ICCD in counts as

$$c(\lambda) = \frac{R_s(\lambda) I_L(\lambda) \cos(\theta_d)}{S(\lambda)} \tag{14}$$

This calibration enables the measurement of absolute spectral irradiance from the plasma (assuming isotropic emission) with the collimated detector due to the diffuse reflection from the surface of the Spectralon disk

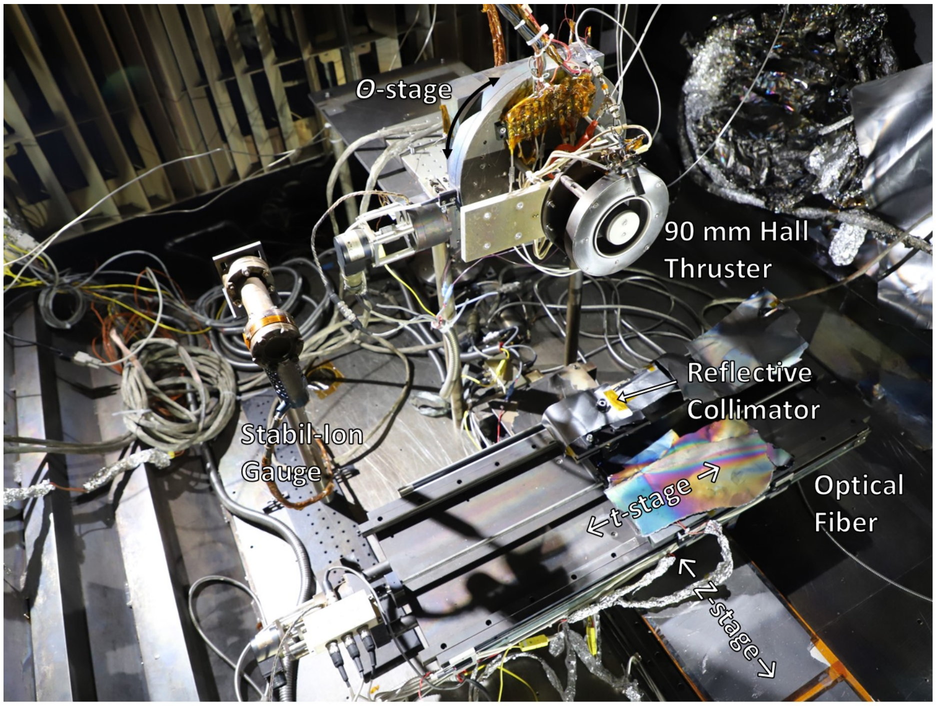

Figure 6: Experimental configuration inside the EP2 vacuum chamber at The Aerospace Corporation.

target.

Results and Discussion

Overview of Data Sets and Thruster Operating Conditions

The original intent of the measurement survey was to compare data for a low and high background pressure case measured at multiple downstream locations. However, due to equipment malfunction and time constraints the scope of the survey was not fulfilled as intended. Three sets of measurements were taken, each at a different thruster operating condition and a different downstream position, making direct comparison of the data sets inconvenient.

The most complete data set acquired was for the elevated background pressure condition where extra xenon gas was leaked into the chamber to raise the background pressure to a factor of five higher than the nominal background pressure. This is the data set that will be shown and discussed in detail in this paper. (The other two data sets had positioning errors that precluded their 2D analysis. However, their 1D analysis is shown in the appendix for reference.) Table 3 summarizes the thruster operating condition, measurement location, and spatial resolution of each data set. The 5× pressure data set was analyzed with 1D (Abel inversion) and 2D (inverse Radon transform) tomographic techniques. The 1D results will be shown first followed by a comparison with the 2D analysis.

Data Set	P (Torr-Xe)	$\dot{m}_a$ (sccm)	$\dot{m}_c$ (sccm)	z (mm)	n_t	Δt (mm)	n_θ	$\Delta\theta$ (deg.)
5× Pressure	7.28×10^{-6}	19.30	2.0	19.1	41	5.1	12	15
Nominal	1.69×10^{-6}	20.94	2.0	12.7	41	6.4	12	15
$\dot{m}_c$=3 sccm	1.43×10^{-6}	19.25	3.0	9.5	41	5.1	12	15

Table 3: Summary of thruster operating condition, measurement location, and resolution for each data set. For all cases, the discharge voltage was 300 V, the anode current was 1.67 A, and the inner and outer magnet currents were 2.0 A. The reported pressure is from the internally mounted Stabil-Ion gauge.

1D Analysis

The irradiance data measured at negative t locations for the $\theta = 90°$ thruster view (Fig. 7a) was used to calculate the the radiant power density, $J_\lambda(r)$, as a function of radius via Abel inversion of the irradiance measurements. This reconstruction corresponded to the non-cathode half of the plume. Neutral excited state density was calculated by multiplying the radiant power density by a constant factor determined from Eq. 9 and plotted in Fig. 7c.

The signal to noise ratio for each peak in the measured spectra was calculated (Fig. 7b) to assess the quality of the measurements as a function of location. A sharp drop in the ratio is seen when the detector is located outside of the acceleration channel region of the plume. For the two weakest lines, at 820.6 and 826.7 nm, the ratios fall below 10 outside of this region and to unity at a radius of 8 cm, suggesting these measurements may not be adequate for the fit to the CRM in regions far outside of the channel.

The CRM was fit to the experimentally measured values of radiant power density to predict electron temperature using two line ratios (823.2/828.0 nm and 834.7/828.0 nm) and three, four, and five line least squares fits as described in Eqs. 6 and 8. The three line fit includes the 823.2, 828.0, and 834.7 nm lines and the four and five line fits add the 820.6 and 826.7 nm lines, respectively. The results of the electron temperature predictions are shown in Fig 7e.

The predicted electron temperature plots exhibit a function with a peak centered on the acceleration channel, which suggests a good performance of the Abel inversion in the calculation of radiant power density. The two line ratio predictions diverge from the multi-line fit predictions beyond the center of the acceleration channel and rise to unreasonably high values just outside of the channel while the multi-line predictions fall to low values. In the case of the 823.2/828.0 nm line ratio, we see from Fig. 2a that at electron temperatures less than 20 eV the model predicts a ratio greater than unity. However, in our radiant power density calculations from tomographic reconstruction, the ratio becomes less than unity at r=6.9 cm and the ratio of the directly measured irradiance is less than unity at r=6.4 cm. This ratio inversion outside of the acceleration channel was also observed in a similar study in Ref. 15 involving the Busek BHT-200 thruster. The electron temperature appears to approach 2 eV in these regions, near the lower limit for which $1s_5$ density ratios are modeled, suggesting an improved model for the $1s_5$ density is required at low temperatures (or one should avoid states linked to the metastable in these cases).

The multi-line least squares fit electron temperature predictions show consistent results. The three line prediction matches closely with 823/828 nm ratio inside the acceleration channel and predicts a peak temperature of 5.9 eV. The four and five line fits are offset lower and predict peak temperatures of 5.2 and 5.5 eV, respectively. The relative errors for the five line CRM fit are plotted in Fig 7f for each emission line. The 826.7 nm peak fit contributes the most error to the overall fit followed by the other low signal line at 820.6 nm for regions inside the channel. The measured irradiance for the 826.7 nm line had higher uncertainty compared to the other measured lines due its low signal and close proximity to the 828.0 nm line, which led to error when integrating its line shape. The least squares fit error for the three and four line fits is plotted in Fig. 12. The three line prediction led to the least overall fit error.

Given the radiant power density and electron temperature, the product of neutral density and electron density, $N_0 N_e$, can be calculated using Eq. 1. Figure 7d shows the density product calculated for the three thruster operating conditions using the excitation rates for the $2p_6$ and $2p_5$ energy levels as a function of electron temperature predicted by the three line fit. Despite the different operating conditions and downstream locations of the measurements, a density product of about 1.5×10^{22} cm^{-6} at the center of the acceleration channel was observed in all three data sets. The elevated background pressure case showed a higher density product on both sides of the channel presumably due to the higher neutral density from the background gas. The density product calculations for the energy level pairs show discrepancy in the regions where electron temperature prediction has a high fit error.

2D Analysis

Irradiance measurements from 12 viewing angles of the thruster, each with 41 measurements along the scanning axis, t, were processed by filtered back projection to calculate the spatially resolved radiant power density, $J_\lambda(x, y)$. Figure 8a shows the 823.2 nm irradiance as a sinogram. Its backprojection was multiplied by a constant factor determined from Eq. 9 to calculate the density of the $2p_6$ state neutral atoms as shown in Fig 8b. The densities of the other neutral excited states are shown in Fig. 9.

These back-projected data exhibit streaks of high intensity emanating from the cathode orifice region.

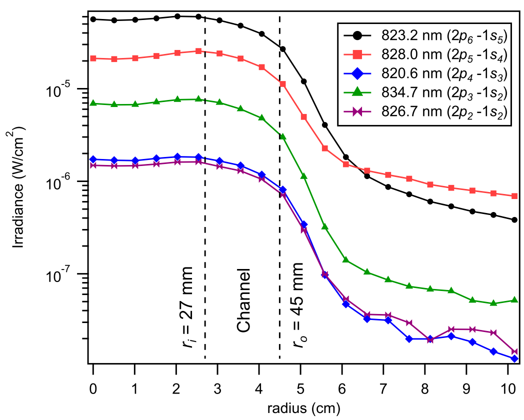

(a) Irradiance of emission lines at detector.

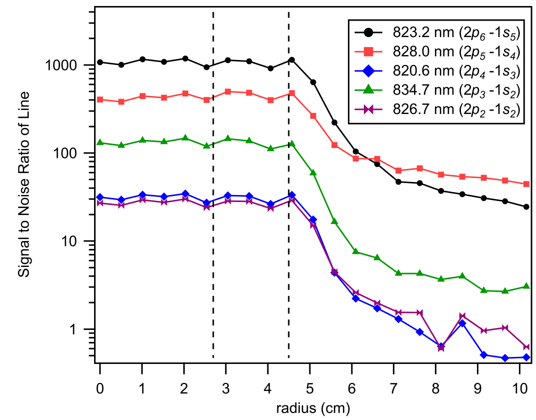

(b) Signal to noise ratio for each emission line in measured spectra.

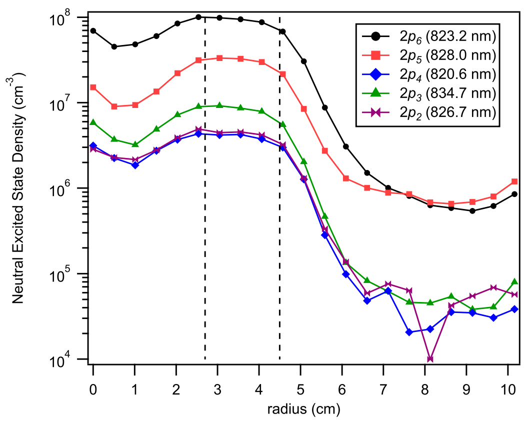

(c) Neutral excited state density calculated using Eq. 9.

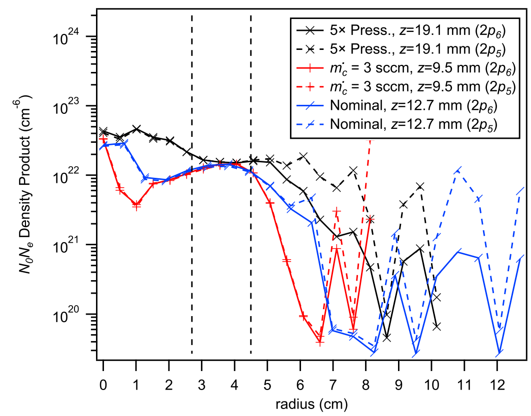

(d) Product of $N_0 N_e$ for the three different test conditions calculated using Eq. 1 with excitation rates for the $2p_6$ and $2p_5$ energy levels as a function of the three line temperature prediction.

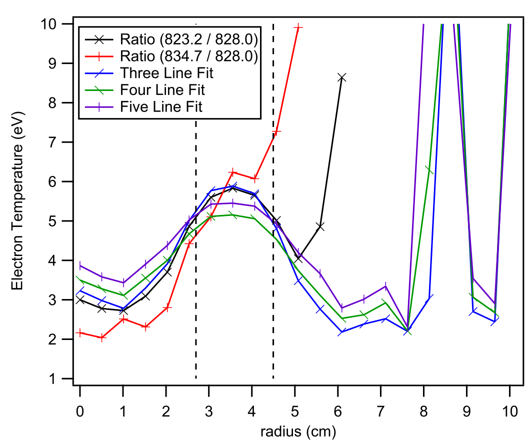

(e) Electron temperature values calculated by fitting the CRM to the experimental data.

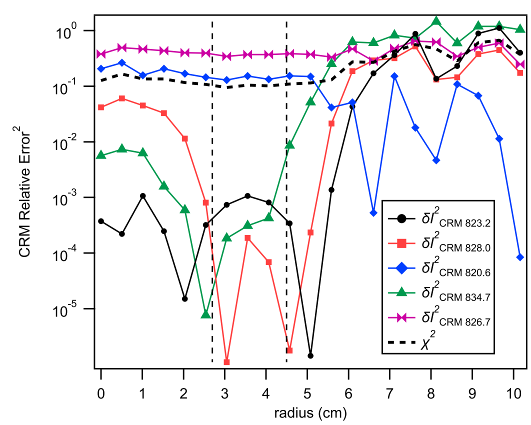

(f) Least squares fit error for the five line temperature fit (see Eq. 8).

Figure 7: One dimensional analysis of the non-cathode half of the plume from the irradiance measurements at negative t locations for $\theta = 90°$ for the 5× pressure condition ($z = 19.1$ mm). The local radiant power density values were found using an Abel inversion of the flux density. The three line electron temperature fit includes the 823.2, 828.0, 834.7 nm lines. The four and five line fits add the 820.6 and 826.7 nm lines, respectively.

The streaks were a numerical artifact of the back projection due to an inadequate number of thruster viewing angles in the irradiance sampling. When a small object approximating a point source such as the cathode emission is under-sampled, a star-shaped pattern of streaks will result as described in Ref. 18. When sampling an object for filtered back projection, the number of projections (viewing angles) should approximately equal the number of rays (lateral measurements), with the ideal ratio of viewing angles to rays being $\pi/2$.[18] These numerical artifacts contributed more prominently in the back projection of the low signal 820.6 and 826.7 nm irradiance. Due to the ratio dependence of the electron temperature prediction, the effects of these artifacts may be somewhat mitigated.

Despite the obscuring effect of the numerical artifacts, an asymmetric high density region was observed in the channel near the cathode orifice at $x = -0.75$, $y = 3.25$ cm for all the measured excited states. Figure 10c shows cross sections of the $2p_6$ state density along $x = 0$ and $y = 0$ plotted with the 1D calculation of the $2p_6$ state density for comparison. The cross section along $y = 0$ traverses the streak artifacts and their effect is seen as irregularities in the plot shape. The $x = 0$ cross section travels along a single streak and has a more regular shape, which matches well with the 1D analysis in shape and magnitude.

The 2D electron temperature prediction from the three line fit is shown in Fig. 10a along with cross sections comparing it to the other multi-line fits, two line ratios, and the 1D analysis (Figs. 10b and 10c). The CRM fit the 2D data inside the channel with reasonable success, but the data outside the channel could not be fit with physically realistic results. The three line temperature prediction along the $x = 0$ cross section shows a $+1.8$ eV offset compared with its 1D analysis. A similar offset is seen for the 823.2/828.0 nm ratio prediction. However, the four and five line fits matched more closely with their 1D analysis and showed offsets of $+1.0$ and $+0.7$ eV, respectively. These offsets are likely due to the numerical artifact streak that runs along $x = 0$. Good agreement is seen among the 2D channel temperature predictions and with the 1D analysis for the negative x side of the $y = 0$ cross section. This region appeared to be mostly not affected by the numerical artifacts unlike the positive x side which shows an irregularly shaped temperature profile.

The temperature predictions corresponding to the cathode orifice location showed some inconsistency. The multi-line fits exhibited a spread of 4.2 eV where the three line prediction was 14.5 eV and the five line prediction was 11.7 eV. The poor fit here is not due to a lack of signal, though it may be related to the insufficient viewing angles for proper back projection. There is a strong possibility the electron energy distribution is non-Maxwellian in this region which would lead to erroneous temperature predictions when applying the present CRM.

Figure 11 displays the temperature predictions inside the channel for all of the CRM fits. The 823.2/828.0 nm ratio and the three line fit show close agreement. The four and five line fits produce predictions that are about 1.5 eV lower. The 834.7/828.0 nm ratio fit was seen to be the poorest quality. An asymmetric region of elevated temperature is consistently observed in the channel adjacent to the cathode orifice occurring at $x = 0.75$, $y = 3.75$ cm, which is opposite in x location to the region of high excited state neutral density. This region of elevated electron temperature was also seen in Langmuir probe measurements for a near-field study[22] of the same thruster plotted in Fig. 11f for comparison. These measurements were for a $2.5\times$ background pressure case and taken at $z = 22.4$ mm. The electron temperature was calculated using the difference between plasma potential and floating potential assuming a Maxwellian electron distribution and Bohm velocity for the ions.

Conclusions and Future Work

Optical emission measurements were taken in the near-field plume of a laboratory Hall effect thruster to evaluate the use of a collisional radiative model in conjunction with tomographic reconstruction techniques to make spatially-resolved electron temperature predictions. Despite the limited resolution of the data set, the results indicate that reasonable predictions can be made in regions near the acceleration channel. However, in regions outside of the channel where the the ratio of 828.0 to 823.2 nm emission was greater than one and the signal to noise ratio of the other measured emission lines was low, the fit of the CRM to the data was problematic.

The biggest limitation to the tomographic aspect of this study was the poor angular sampling resolution of the irradiance data sets, which led to numerical artifacts when radiant power density was reconstructed via filtered back projection. These star-patterned streaks led to irregularities that limited the applicability of the CRM fit to the data resulting in regions of increased electron temperature predictions in regions corresponding the artifacts. Despite the effect of the numerical artifacts, an asymmetric electron temperature region near

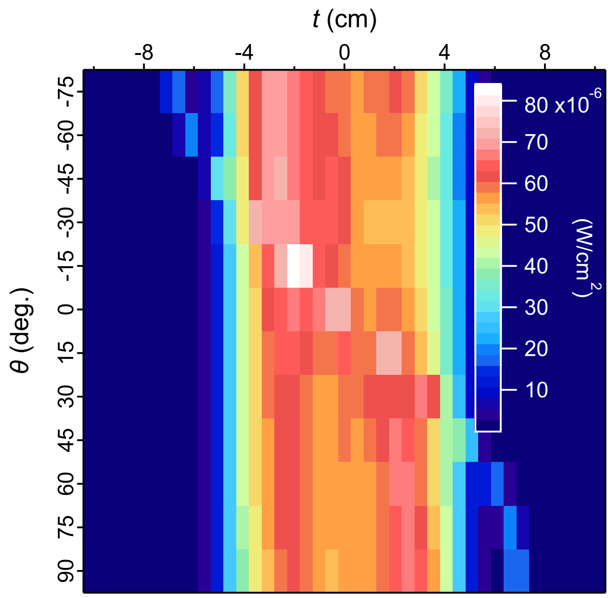

(a) Irradiance of 823.2 nm line at detector as a function of thruster rotation angle and detector position. (Displayed as a sinogram.)

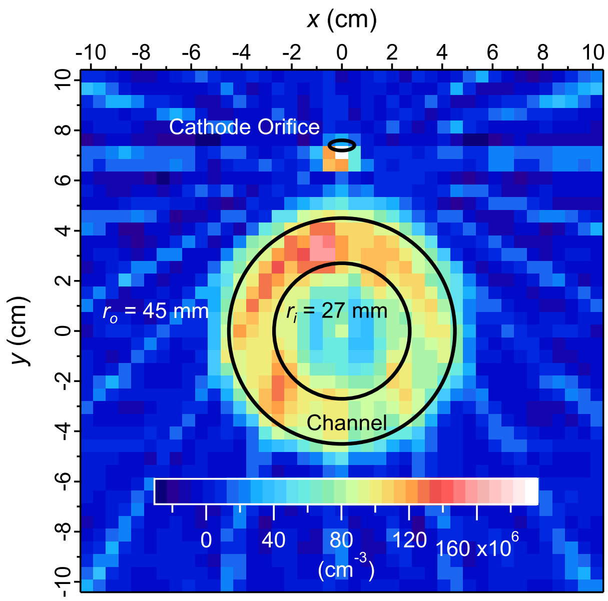

(b) Density of $2p_6$ state calculated using the inverse radon transform of irradiance data.

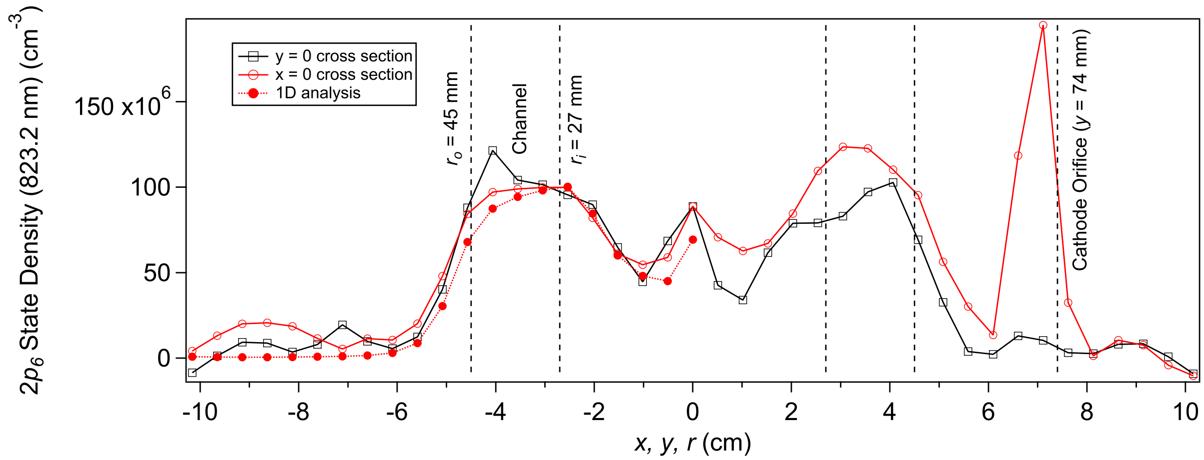

(c) Cross sections of the $2p_6$ state density compared with the 1D analysis.

Figure 8: Irradiance at 823.2 nm was measured for twelve thruster rotational positions and was used to reconstruct a two dimensional data set of radiant power density via the filtered back projection method. These 2D data were used to find the excited state density and predict electron temperature using the CRM.

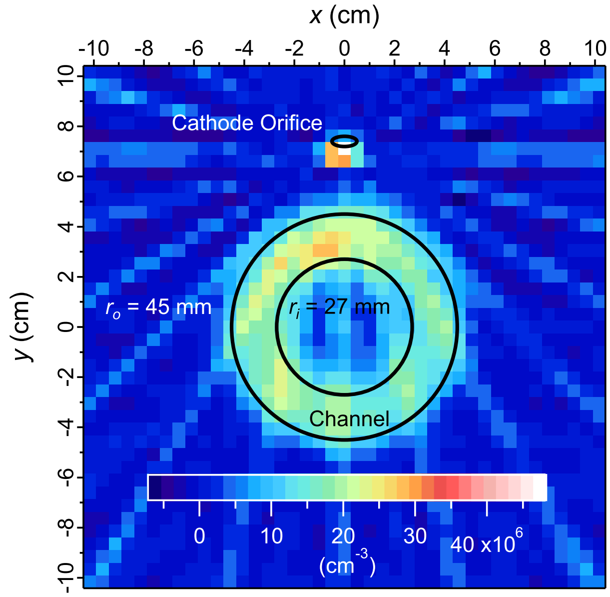

(a) Density of $2p_5$ state calculated using the inverse radon transform of the 828.0 nm irradiance data.

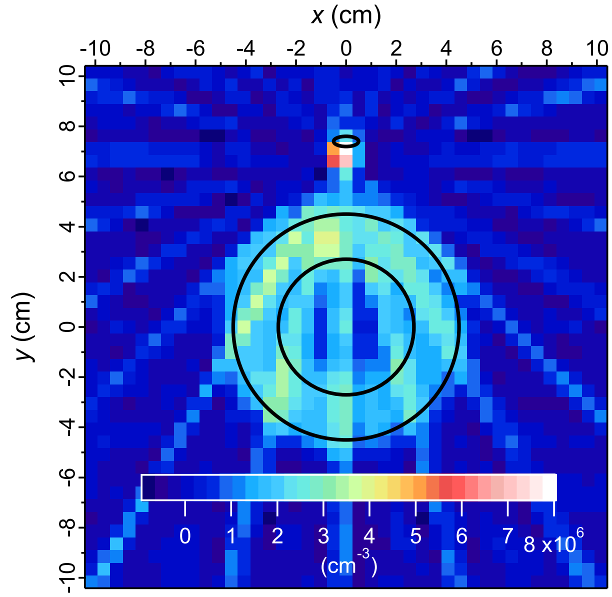

(b) Density of $2p_4$ state calculated using the inverse radon transform of the 820.6 nm irradiance data.

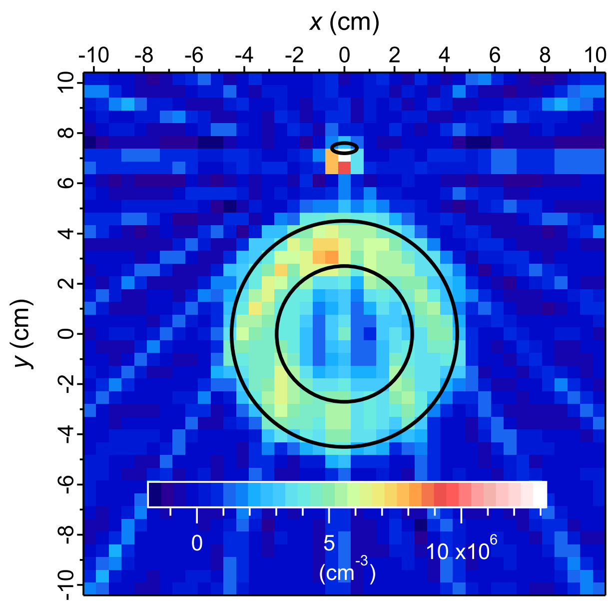

(c) Density of $2p_3$ state calculated using the inverse radon transform of the 834.7 nm irradiance data.

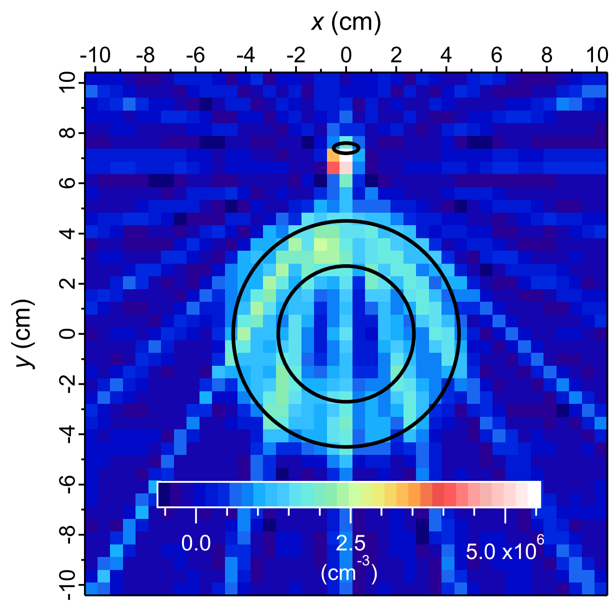

(d) Density of $2p_2$ state calculated using the inverse radon transform of the 826.7 nm irradiance data.

Figure 9: Neutral excited state density calculated from the inverse radon transform of the irradiance measurements.

the cathode plasma bridge was resolved and corroborated with Langmuir probe measurements from another study.

A future study with a higher spatial sampling resolution and a more ideal ratio of viewing angles to number of lateral measurements of at least unity will enable the asymmetries of the cathode plasma bridge to be studied in greater detail. One of the challenges with the present experimental setup was the time required to complete a set of measurements. The long ICCD integration times required due to the low signal throughput of the the optics, led to a data acquisition time of about three hours for the sparse data

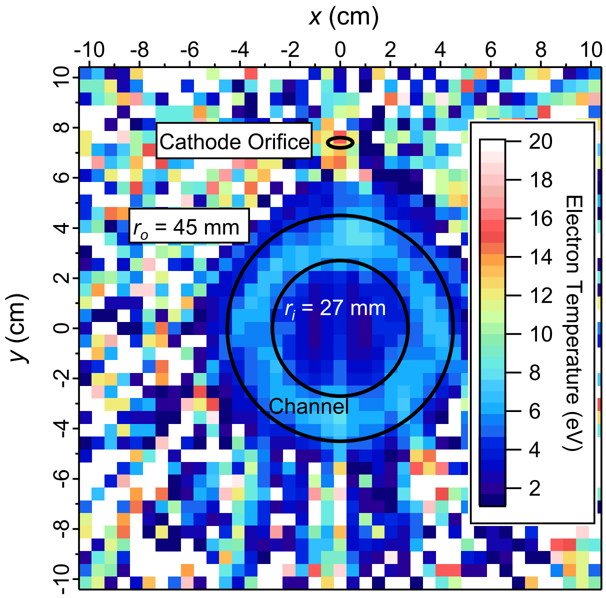

(a) Electron temperature prediction from three line fit of 2D radiant power density derived from the filtered back projection of irradiance measurements.

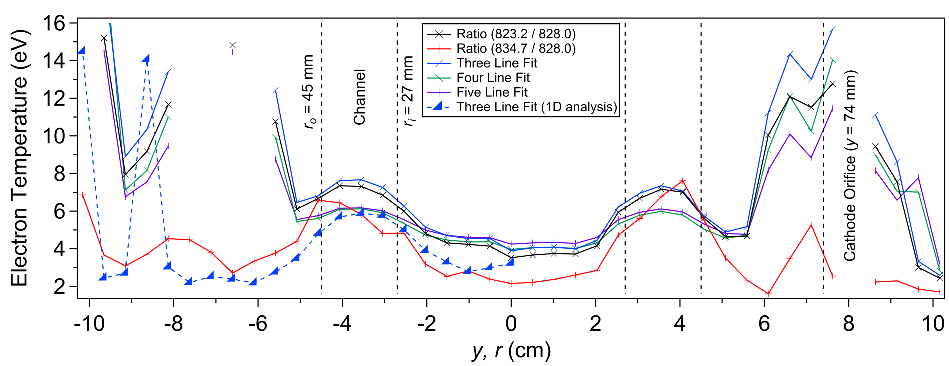

(b) Cross sectional comparison of the 2D electron temperature predictions for the $x = 0$ cross section. The 1D three line temperature fit is also plotted for comparison.

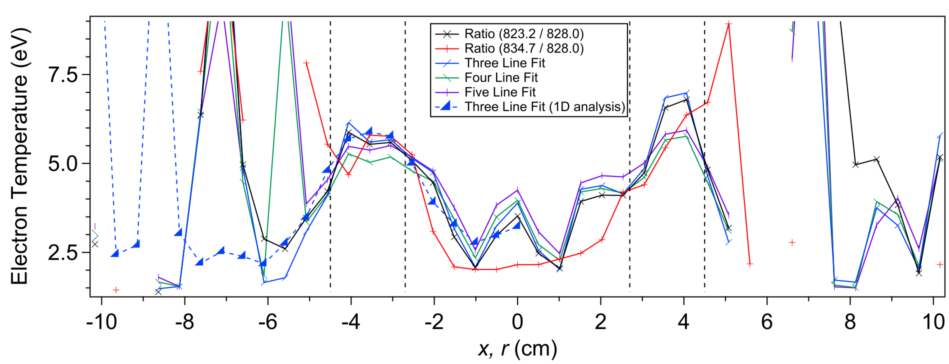

(c) Cross sectional comparison of the 2D electron temperature predictions for the $y = 0$ cross section. The 1D three line temperature fit is also plotted for comparison.

Figure 10: Electron temperature prediction from three line fit of 2D radiant power density and cross sectional comparison of temperature predictions from other multi-line fits for the $5\times$ pressure condition ($z = 19.1$ mm). The three line fit includes the 823.2, 828.0, 834.7 nm lines. The four and five line fits add the 820.6 and 826.7 nm lines, respectively.

set presented here. A future experiment is planned that will use optical bandpass filters in place of the spectrometer and a photo multiplier tube with relatively high quantum efficiency in the near infrared in place of the ICCD to enable quicker data acquisition allowing a higher sampling resolution. Future work will look to extend the CRM to accept more complicated electron energy distributions than a single Maxwellian by leveraging differences in the $2p$ excitation cross section shapes at high energies to provide insight into how electron energy distribution varies in different regions of the plume and with proximity to the cathode.

Acknowledgments

The authors would like to thank John Nocerino of The Aerospace Corp. for his advice on the calibration of the optical system and for the use of various optical components. Also, thanks goes to Rainer Dressler of Spectral Sciences, Inc. for providing metastable fraction predictions for use with the CRM and John Boffard from the University of Wisconsin Madison for providing tabulated experimentally measured excitation cross section data.

References

[1]Chiu, Y., Austin, B. L., Williams, S., Dressler, R. A., and Karabadzhak, G. F., "Passive Optical Diagnostic of Xe-Propelled Hall Thrusters. I. Emission Cross Sections," *Journal of Applied Physics*, Vol. 99, No. 11, 2006.

[2]Stangeby, P. C., "Determination of T_e from a Langmuir probe in a magnetic field by directly measuring the probe's sheath drop using a pin-plate probe," *Plasma Physics and Controlled Fusion*, Vol. 37, No. 11, November 1995, pp. 1337–1347.

[3]Kunze, H.-J., *Introduction to Plasma Spectroscopy*, Springer Series on Atomic, Optical, and Plasma Physics (Book 56), Springer, 2009.

[4]Karabadzhak, G. F., Chiu, Y., and Dressler, R. A., "Passive optical diagnostic of Xe propelled Hall thrusters. II. Collisional-radiative model," *Journal of Applied Physics*, Vol. 99, No. 11, 2006, pp. 113305.

[5]Dressler, R. A., Chiu, Y., Zatsarinny, O., Bartschat, K., Srivastava, R., and Sharma, L., "Near-Infrared Collisional Radiative Model for Xe Plasma Electrostatic Thrusters: The Role of Metastable Atoms," *Journal of Physics D: Applied Physics*, Vol. 42, No. 18, August 2009.

[6]Kramida, A., Yu. Ralchenko, Reader, J., and NIST ASD Team, NIST Atomic Spectra Database (ver. 5.6.1), Available: `https://physics.nist.gov/asd`. National Institute of Standards and Technology, Gaithersburg, MD., 2018.

[7]Fons, J. T. and Lin, C. C., "Measurement of the cross sections for electron-impact excitation into the $5p^5 6p$ levels of xenon," *Physical Review A*, Vol. 58, No. 6, Dec. 1998, pp. 4603–4615.

[8]Mitchner, M. and Kruger, C. H., *Partially Ionized Gases*, John Wiley & Sons, Inc., 1973.

[9]Sommerville, J. D., King, L. B., Chiu, Y.-H., and Dressler, R. A., "Ion-Collision Emission Excitation Cross Sections for Xenon Electric Thruster Plasmas," *Journal of Propulsion and Power*, Vol. 24, No. 4, July 2008, pp. 880–888.

[10]Jung, R. O., Boffard, J. B., Anderson, L. W., and Lin, C. C., "Electron-impact excitation cross sections from the xenon $J = 2$ metastable level," *Phys. Rev. A*, Vol. 72, A 2005.

[11]Allan, M., Zatsarinny, O., and Bartschat, K., "Near-threshold absolute angle-differential cross sections for electron-impact excitation of argon and xenon," *Phys. Rev. A*, Vol. 74, Sept. 2006, pp. 030701.

[12]Srivastava, R., Stauffer, A. D., and Sharma, L., "Excitation of the metastable states of the noble gases," *Phys. Rev. A*, Vol. 74, July 2006, pp. 012715.

[13]Allan, M., Zatsarinny, O., and Bartschat, K., "Near-threshold absolute angle-differential cross sections for electron-impact excitation of argon and xenon," *Phys. Rev. A*, Vol. 74, No. 3, Sept. 2006, pp. 030701.

[14]Ton-That, D. and Flannery, M. R., "Cross sections for ionization of metastable rare-gas atoms (Ne*, Ar*, Kr*, Xe*) and of metastable N_2*, CO* molecules by electron impact," *Phys. Rev. A*, Vol. 15, No. 2, Feb. 1977, pp. 517–526.

[15]Matlock, T., Hargus, Jr., W., Larson, C., and Nakles, M., "Inversion Method for Reconstructing Hall Thruster Plume Parameters from Optical Measurements," *Proceedings of the 43rd AIAA/ASME/SAE/ASEE Joint Propulsion Conference*, 2007, AIAA-2007-5303.

[16]Gonzales, A. E., Hargus Jr., W. A., and Nakles, M. R., "Non-Intrusive, Time-Resolved Hall Thruster Near-Field Electron Temperature Measurements," *Proceedings of the 47th AIAA/ASME/SAE/ASEE Joint Propulsion Conference*, 2011, AIAA 2011-5587.

[17]Pretzier, G., Jager, H., Neger, T., Philipp, H., and Woisetschlager, J., "Comparison of Different Methods of Abel Inversion Using Computer Simulated and Experimental Side-On Data," *Zeitschrift für Naturforschung*, Vol. 47a, 1992, pp. 955–970.

[18]Kak, A. C. and Slaney, M., *Principles of Computerized Tomographic Imaging*, IEEE Press, 1988.

[19]Raitses, Y., Dorf, L. A., Litvak, A. A., and Fisch, N. J., "Plume reduction in segmented electrode Hall thruster," *Journal of Applied Physics*, Vol. 88, No. 3, Aug. 2000, pp. 1263–1270.

[20]Diamant, K. D., Spektor, R., Beiting, E. J., Young, J. A., and Curtiss, T. J., "The Effects of Background Pressure on Hall Thruster Operation," *Proceedings of the 48th AIAA/ASME/SAE/ASEE Joint Propulsion Conference*, 2012, AIAA 2012-3735.

[21]Diamant, K. D., Lee, T., Liang, R., Noland, J., Vial, V., and Cornu, N., "Performance and Plume Characterization of the PPS 1350-G Hall Thruster," *52nd AIAA/SAE/ASEE Joint Propulsion Conference*, 2016, AIAA 2016-4543.

[22]Matlock, T. S., Nakles, M. R., and Spektor, R., "Pressure Dependence of Near-Field Plume Properties in a 1kW Laboratory Hall Thruster," *Proceedings of the 35th International Electric Propulsion Conference*, 2017, IEPC-2017-20.

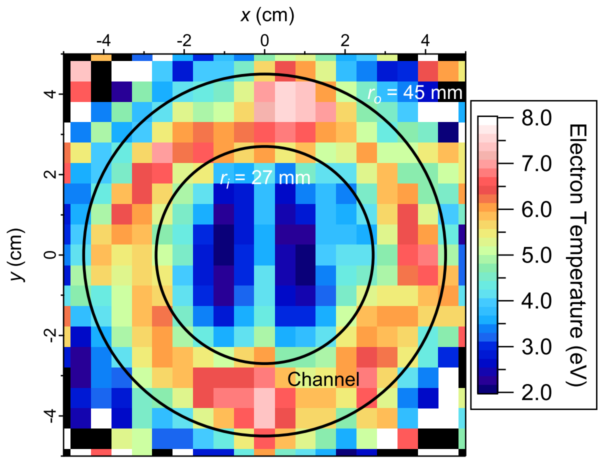

(a) Ratio 823.2/828.0 nm.

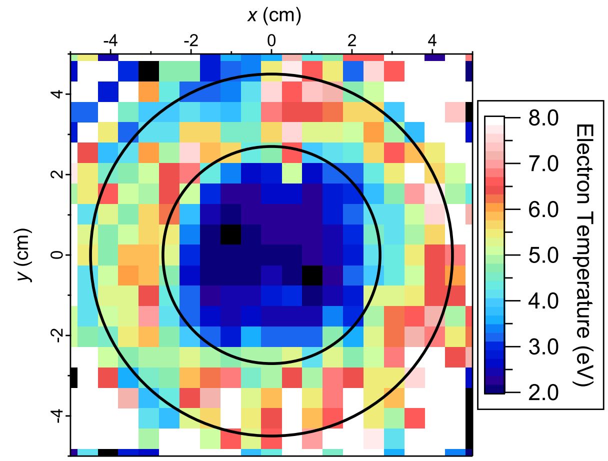

(b) Ratio 834.7/828.0 nm.

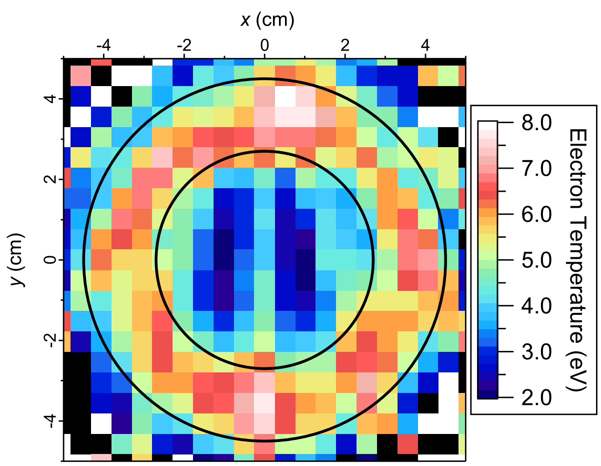

(c) Three line fit.

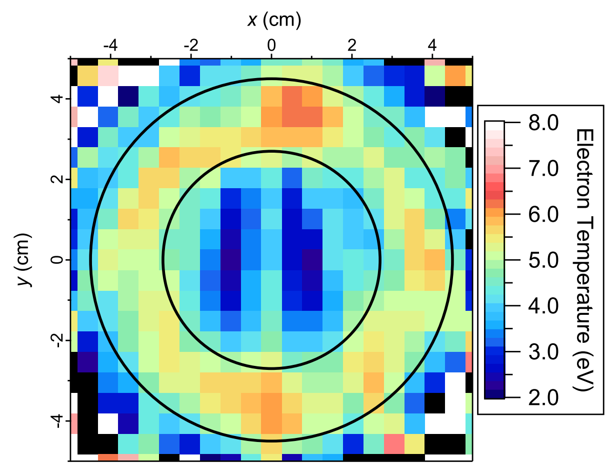

(d) Four line fit.

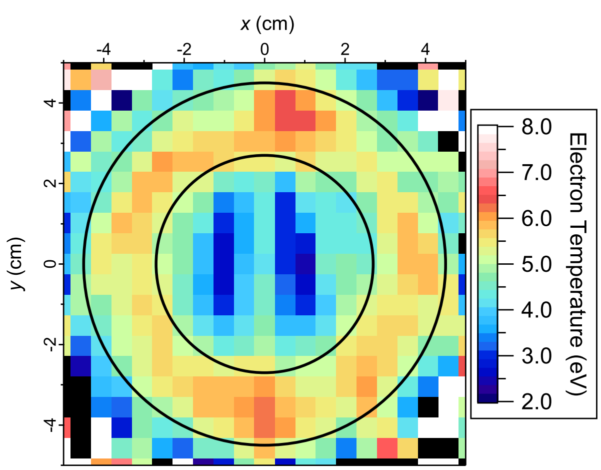

(e) Five line fit.

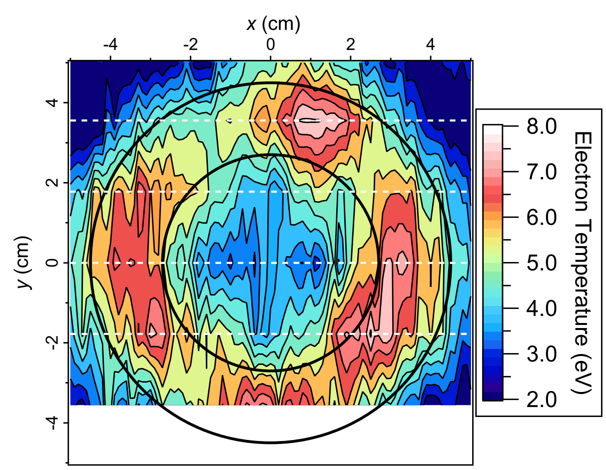

(f) Langmuir probe data.

Figure 11: Two dimensional electron temperature predictions in the acceleration channel region of the plume for the 5× pressure condition (z = 19.1 mm). The three line fit includes the 823.2, 828.0, 834.7 nm lines. The four and five line fits add the 820.6 and 826.7 nm lines, respectively. The Langmuir probe data is from a near-field pressure effects study[22] for a 2.5× background pressure condition at z=22.4 mm.

Appendix

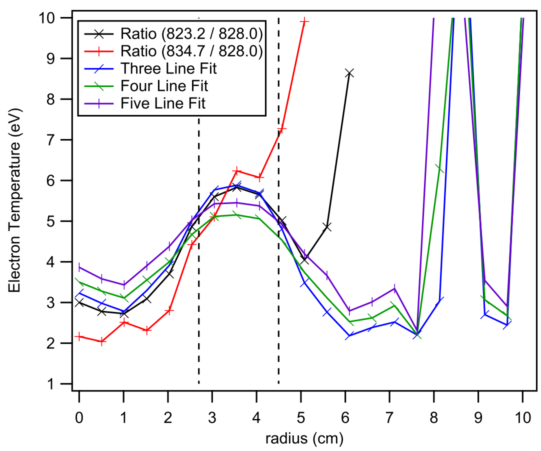

(a) Electron temperature values calculated by fitting the CRM to the experimental data.

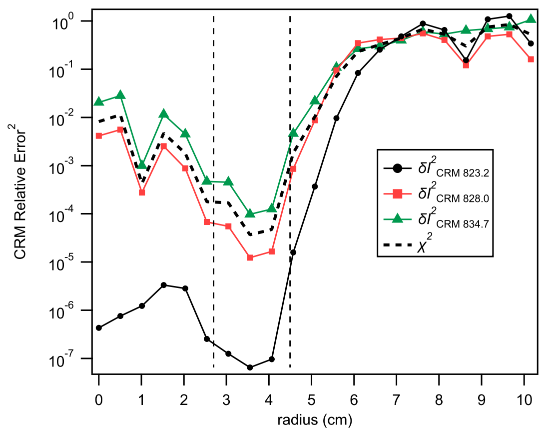

(b) Least squares fit error for the three line temperature fit (see Eq. 8).

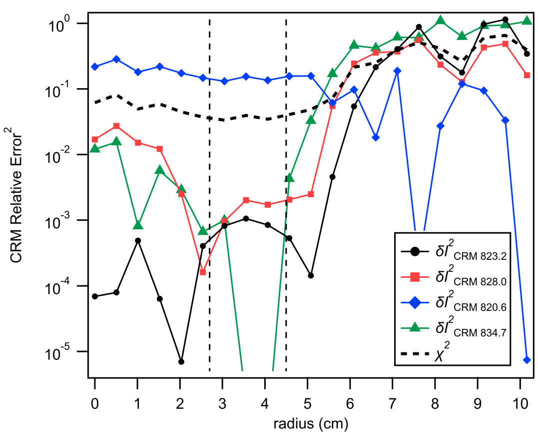

(c) Least squares fit error for the four line temperature fit (see Eq. 8).

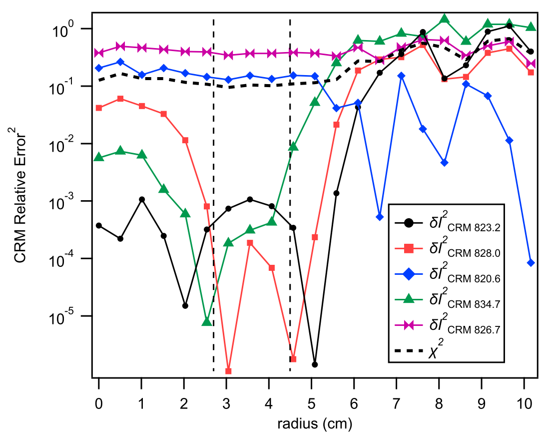

(d) Least squares fit error for the five line temperature fit (see Eq. 8).

Figure 12: Least squares electron temperature fits for one dimensional data analysis of the 5× pressure condition ($z = 19.1$ mm). The three line fit includes the 823.2, 828.0, 834.7 nm lines. The four and five line fits add the 820.6 and 826.7 nm lines, respectively.

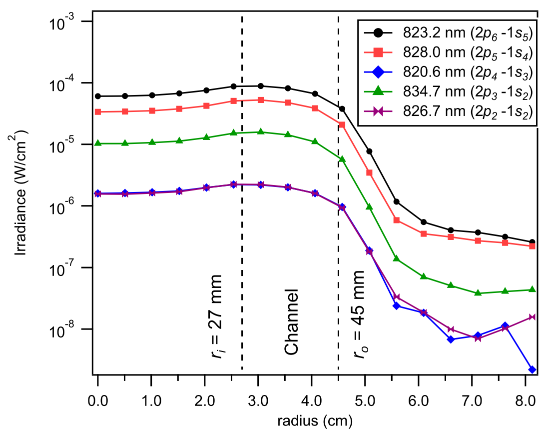

(a) Irradiance of emission lines at detector.

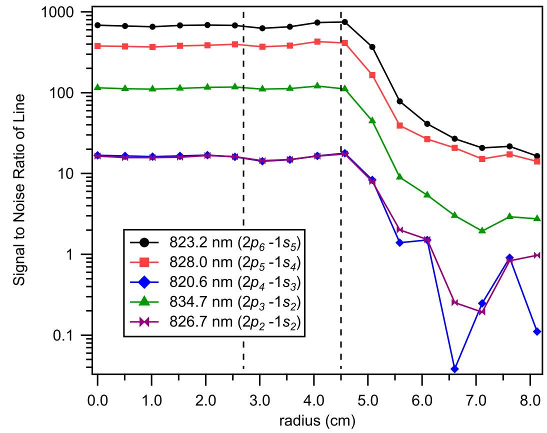

(b) Signal to noise ratio for each emission line in measured spectra.

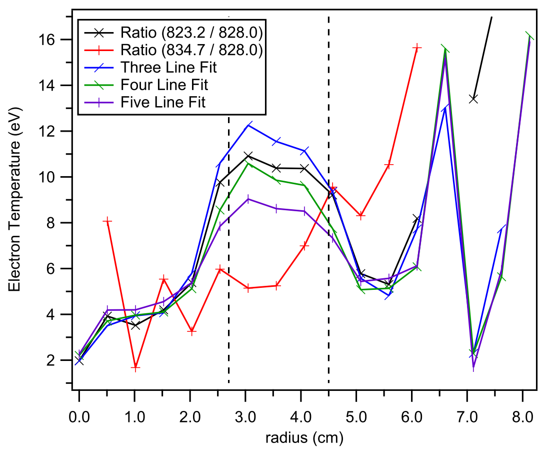

(c) Electron temperature values calculated by fitting the CRM to the experimental data.

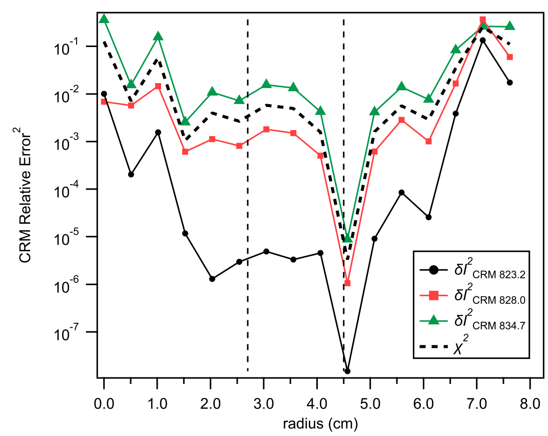

(d) Least squares fit error for the three line temperature fit (see Eq. 8).

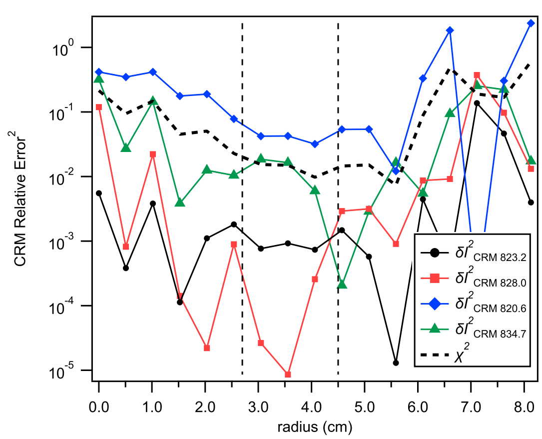

(e) Least squares fit error for the four line temperature fit.

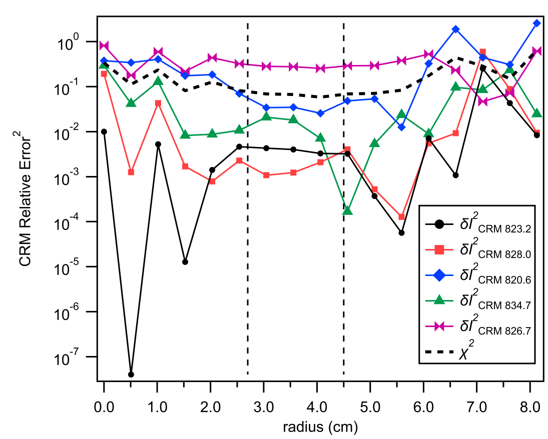

(f) Least squares fit error for the five line temperature fit.

Figure 13: Irradiance measurements and least squares electron temperature fits for one dimensional data analysis of the $\dot{m}_c = 3$ sccm condition ($z = 9.5$ mm). The three line fit includes the 823.2, 828.0, 834.7 nm lines. The four and five line fits add the 820.6 and 826.7 nm lines, respectively.

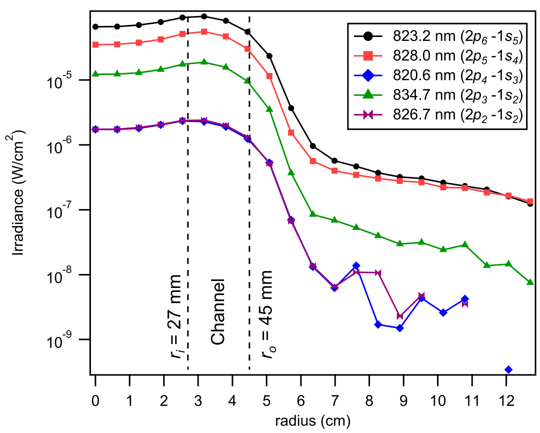

(a) Irradiance of emission lines at detector.

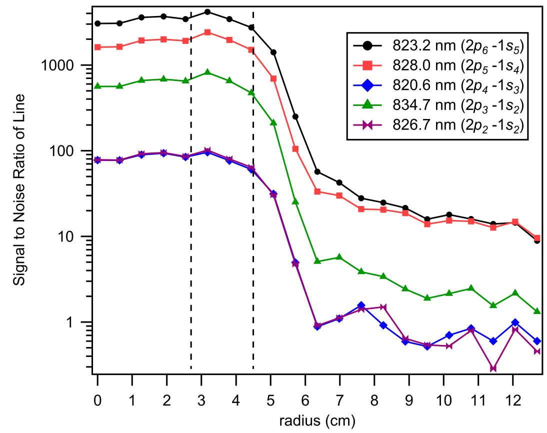

(b) Signal to noise ratio for each emission line in measured spectra.

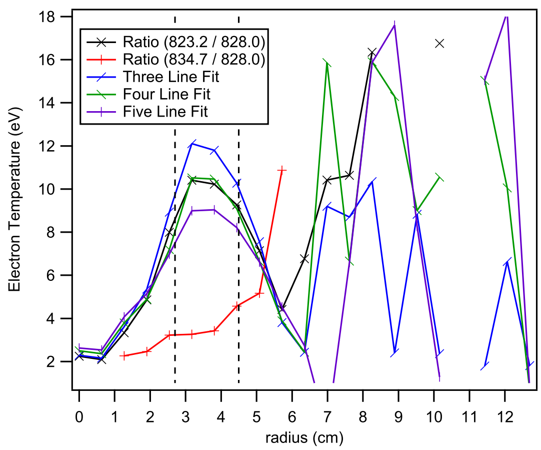

(c) Electron temperature values calculated by fitting the CRM to the experimental data.

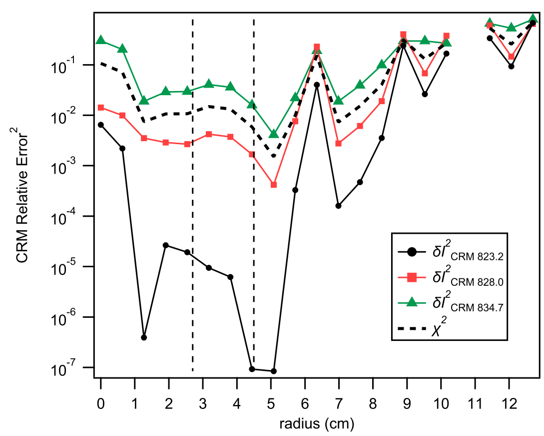

(d) Least squares fit error for the three line temperature fit (see Eq. 8).

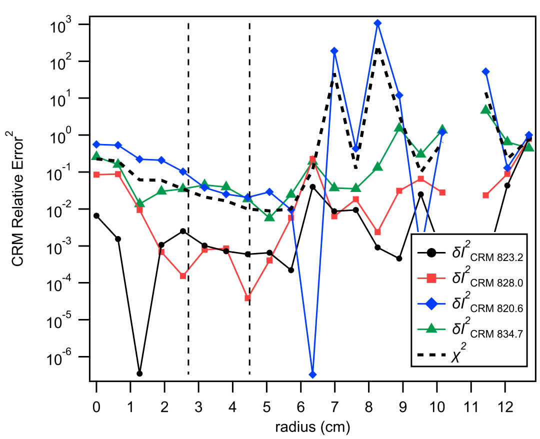

(e) Least squares fit error for the four line temperature fit.

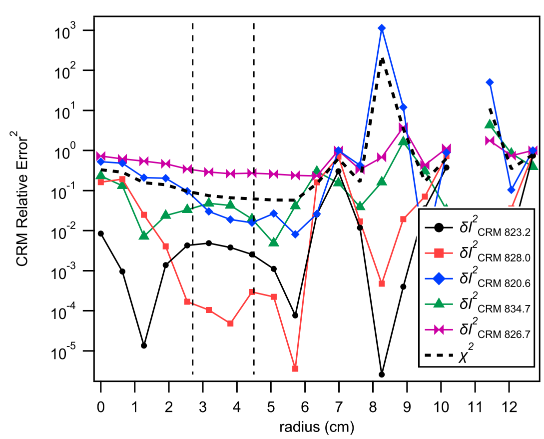

(f) Least squares fit error for the five line temperature fit.

Figure 14: Irradiance measurements and least squares electron temperature fits for one dimensional data analysis of the nominal condition ($z = 12.7$ mm). The three line fit includes the 823.2, 828.0, 834.7 nm lines. The four and five line fits add the 820.6 and 826.7 nm lines, respectively.